

Available online at www.sciencedirect.com

jmr&t
Journal of Materials Research and Technology

journal homepage: www.elsevier.com/locate/jmrt

Multi-materials additive manufacturing of Ti64/Cu/316L by electron beam freeform fabrication

Guoqiang Zhu ^a, Liang Wang ^{a,b,*}, Binbin Wang ^{a,b,**}, Binqiang Li ^c,
 Junbo Zhao ^d, Bao Ding ^d, Ran Cui ^a, Botao Jiang ^a, Chunzhi Zhao ^a,
 Baoxian Su ^a, Liangshun Luo ^a, Ruirun Chen ^a, Yanqing Su ^a, Jingjie Guo ^a

^a National Key Laboratory for Precision Hot Processing of Metals, School of Materials Science and Engineering, Harbin Institute of Technology, Harbin 150001, China

^b Zhengzhou Research Institute, Harbin Institute of Technology, Zhengzhou 450000, China

^c Western Superconducting Technologies Co., Ltd., Shaanxi Province Engineering Laboratory for Aerial Material, Xi'an 710018, China

^d NO.703 Research Institute of China State Shipbuilding Company Limited, Harbin 150036, China



ARTICLE INFO

Article history:

Received 19 August 2023

Accepted 19 September 2023

Available online 22 September 2023

Keywords:

Multi-material

Electron beam freeform fabrication

Titanium alloy

Interfacial microstructure

Shear strength

ABSTRACT

Titanium/steel multi-material, given full play to their superiorities, has tremendous value for parts exposed to complexity service environments, yet invariably, its common joining techniques are lack of design freedom. To this end, we employ electron beam freeform fabrication (EBF³) to successfully prepare this multi-material system for the first time, whose interfacial microstructure and property are systematically investigated. Applying Cu as an interlayer, instead of causing extensive cracking and delamination at the interface of Ti64/316L, can effectively suppress the formation of continuous Fe–Ti intermetallic compounds (IMCs), and thus improve the strength of Ti64/Cu/316L interfaces. For the Cu/316L interface, besides the characteristic spherical Cu-rich and Fe-rich solid solutions, a few Fe–Ti IMCs appear within the Fe-rich solid solutions owing to the long-range diffusion of minor Ti atoms. Correspondingly, the dendritic Cu-rich solid solutions can also be found at the Ti64/Cu interface, which is regarded as a critical interface due to the concomitant of complex Cu–Ti IMCs. These Cu–Ti IMCs have less negative effect on the Ti64/Cu interface property relative to Fe–Ti IMCs, and the local strain produced by the deformed α -Ti near the interface and Cu-rich solid solutions can effectively relieve the concentration of residual stress. Consequently, the Ti64/Cu interface exhibits maximum micro-hardness to 490 HV and superior shear strength to 196.5 ± 2.2 MPa, which was attributed to the reinforcement for the tip of keyhole molten pool, as well as the synergy between Cu-rich solid solution and interdendritic Cu–Ti IMCs.

© 2023 The Author(s). Published by Elsevier B.V. This is an open access article under the CC BY-NC-ND license (<http://creativecommons.org/licenses/by-nc-nd/4.0/>).

* Corresponding author. National Key Laboratory for Precision Hot Processing of Metals, School of Materials Science and Engineering, Harbin Institute of Technology, Harbin 150001, China.

** Corresponding author. National Key Laboratory for Precision Hot Processing of Metals, School of Materials Science and Engineering, Harbin Institute of Technology, Harbin 150001, China.

E-mail addresses: wliang1227@hit.edu.cn (L. Wang), binbinwang@hit.edu.cn (B. Wang).

<https://doi.org/10.1016/j.jmrt.2023.09.194>

2238-7854/© 2023 The Author(s). Published by Elsevier B.V. This is an open access article under the CC BY-NC-ND license (<http://creativecommons.org/licenses/by-nc-nd/4.0/>).

1. Introduction

The titanium alloy is an important high-strength metal, which is widely used in national defense, nuclear energy, shipbuilding, electronics, petroleum, chemical and other industrial fields because of its excellent comprehensive performance [1–3]. However, the expensive price and easy oxidation limit the promotion and application of titanium alloys [4]. The austenitic stainless steel is the most commonly used structural material, not only has good mechanical properties, weldability, thermal stability, but the cost is relatively low. Therefore, the combination of high-performance titanium alloys and low-cost stainless steels can meet both performance and economic needs, which provides many advantages in fields such as heat exchangers in chemical, microelectronics, medical, nuclear, thermal power plants, aerospace, etc [5–7]. Traditionally, the composite structures for titanium alloy and stainless steel are mainly achieved through joining technology, such as electron beam welding [8], laser welding [9], diffusion bonding [10,11], explosive welding [12], friction welding [13], brazing welding [14]. However, these joining techniques have the certain requirements for welding position and joining tools, and it is difficult to join complex structural surfaces. Fortunately, the inflexibility of joining can be potentially solved through additive manufacturing (AM) technology, as components can be partitioned into several layers regardless of the complexity and manufactured by stacking layers on top of each other [15].

As known, it is fairly difficult to successfully develop immiscible multi-materials (e.g., titanium alloy and stainless steel) regardless of welding or AM methods. The remarkable differences in physical and chemical properties (e.g., the coefficient of linear expansion and thermal conductivity listed in Table 1) between titanium alloy and stainless steel determine complexity for fabricating titanium/steel multi-materials. Moreover, owing to extremely limited mutual solubility of Fe and Ti, the formation of hard and brittle Fe–Ti IMCs, which are greatly susceptible to cracking, is a critical disadvantage for bonding strength at interface. Chen et al. [16], fabricated Ti64/316L gradient materials by double-wire AM, and found that the content of Fe–Ti IMCs varied with composition, which resulted in severe macro-cracks finally. Rashkovets et al. [17] reported that delamination and cracks emerged at Ti64/316L interface due to the formations of Fe–Ti IMCs. Similarly, Su et al. [18] observed that the more 316L powder mixed in Ti64 before laser melting deposition (LMD), the more Fe–Ti IMCs were formed and eventually caused material cracking.

In this regard, the direct connection of titanium alloys and stainless steel is not popular with the unsatisfied mechanical property of multi-material. There is a common scheme for AM

to mitigate performance differences between layers and impede the formation of Fe–Ti IMCs by adding one or several interlayers, such as Cu [19–21], Ni [22], V [23,24], Ag [25], Nb [23,26], Al [27]. Meng et al. [28] reported that the crack-free titanium/steel gradient materials was fabricated using Inconel 625 as an intermediate layer combined with simultaneous laser preheating. However, Reichardt et al. [29] observed cracking and delamination at compositional mix of 75% V and 25% 316L powders due to the combined effect of FeTi and σ phase. Li et al. [30] deposited V, Cr and Fe interlayers in sequence between Ti64 and 316L, and successfully prepared defect-free titanium steel material by LMD technique, which exhibited excellent mechanical properties. Onuike et al. [31] found that an interlayer Nb between Ti64 and 316L presented a good resistance to crack expansion at interface. In addition, the feasibility of Cu as an interlayer between Ti64 and 316L has also been demonstrated by researchers in Singapore [32], who achieved an overall material tensile strength in excess of 500 MPa via fusing Cu interlayer of approximately 0.5 mm by selective laser melting (SLM). This was attributed to the lack of Fe–Ti IMCs and the presence of α' -Ti at the interface that could deflect cracks from the brittle interface towards the ductile interlayer.

In this work, an attempt is made to achieve titanium/steel multi-material fabrication for the first time with electron beam freeform fabrication (EBF³). The investigation firstly focus on the interfacial microstructure of Ti64/316L multi-material prepared by EBF³, which aim to understand the extent of interfacial damage of EBF³-fabricated Ti64/316L multi-material. Subsequently, the interfacial microstructure and mechanical properties of Ti64/Cu/316L multi-materials are investigated using Cu as an interlayer to further reveal the bonding mechanism, which is contributed to extend the scope for AM with wire as feedstock applications.

2. Experimental procedure

2.1. Materials

A schematic diagram of Ti64/Cu/316L multi-materials deposition process and macro-morphology are shown in Fig. 1. Table 1 lists the basic physical properties of Ti64, 316L and Cu. The 316L stainless steel wire and Cu wire with diameters of 1.0 mm and 1.6 mm were selected as the feedstock, respectively. The Ti64 rolled sheet with a size of 100 mm × 150 mm × 10 mm was used as substrate. The chemical compositions for raw materials are displayed in Table 2. The wires and substrate were polished, pickled and acetone wiped to remove surface oil and oxides, followed heating in a drying oven at 60 °C for 4 ~ 6 h to remove residual moisture. Then, the Ti64/316L multi-materials were

Table 1 – Basic physical properties of Ti64, 316L and pure Cu.

Materials	Density /g·cm ⁻³	Melting point/°C	Expansion /10 ⁻⁶ ·K ⁻¹	Thermal conductivity /W·m ⁻¹ ·K ⁻¹	Thermal diffusion /10 ⁻⁶ ·m ² ·s ⁻¹
Ti6Al4V	4.55	1725	7.14	7.96	2.0
SS316L	8.9	1375	16	21.5	4.0
Cu	8.96	1084	8.3	401	1800

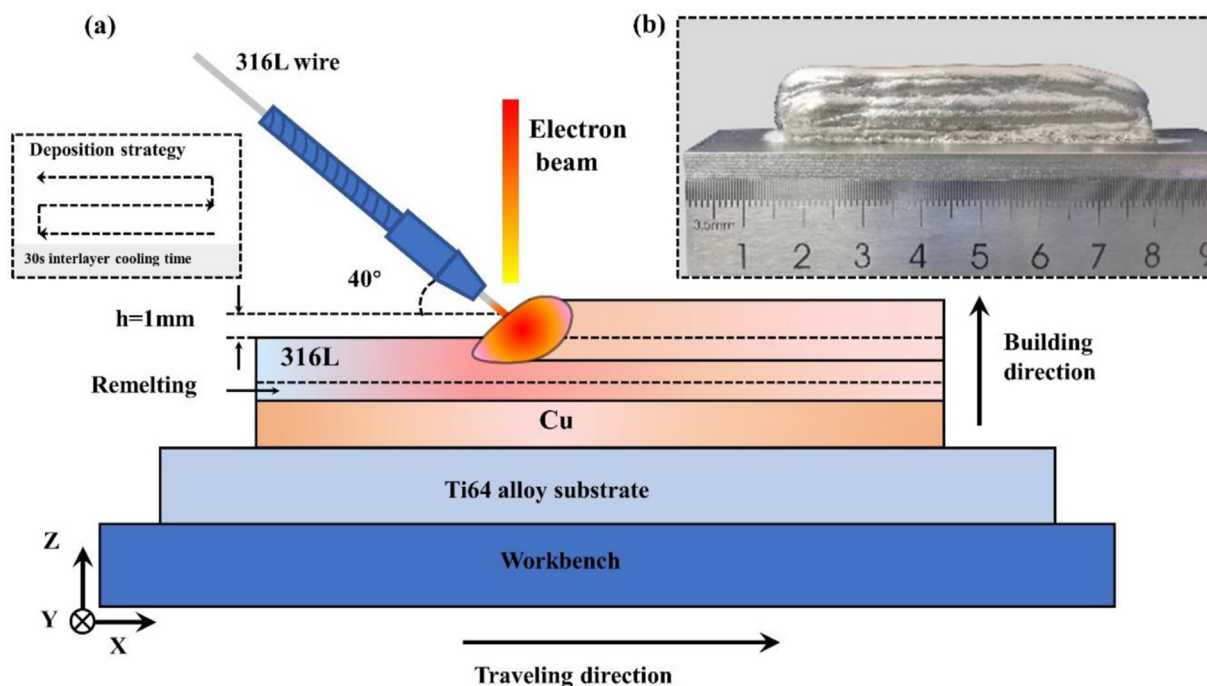


Fig. 1 – The schematic diagram of EBF³-fabricated process and corresponding Ti64/Cu/316L deposit: (a) EBF³-fabricated process; (b) macro-morphology of as-deposited multi-material.

fabricated by EBF³ equipment (Xi'an DMAMS, China) with deposition strategy of multi-pass multilayers under vacuum atmosphere (below 7×10^{-2} Pa). As known, the beam current, scanning speed and feeding speed are dominated parameters for EBF³ technique that have a significant impact on the deposition quality. Table 3 lists the specific parameters for depositing 316L on Ti64 substrate. Subsequently, the Cu was combined between Ti64 and 316L, which was beneficial to restrain the formation of Fe-Ti IMCs. The optimized parameters for depositing Cu on Ti64 substrate and 316L on solidified Cu are displayed in Table 3 to further enhance the barrier effect of Cu. It should be noted that before feeding wires, the electron beam current with 25 mA was set to preheat the surface for the Ti64 substrate by repeatedly remelting 4–5 times to strengthen the bonding of interfacial heterogeneous materials.

2.2. Characterization and test

The samples were extracted from Ti64/Cu/316L multi-materials by electrical discharge machining (X-axis and Z-axis are scanning direction and building direction, respectively, as shown in Fig. 1), which were grounded and polished. The X-ray diffraction (XRD, Panalytical Empyrean)

with Cu-K α radiation was conducted to identify the phases constitution of Ti64/316L, Ti64/Cu and Cu/316L interfaces at 40 kV and 40 mA with a scan angle range (2θ) from 20° to 100°. The electron probe microscope analysis (EPMA, JEOL JXA 8230) with wavelength dispersive spectrometry was applied to characterize the elemental content of micro-composition and elemental concentration distribution of Ti64/Cu and Cu/316L interfaces. The Ti64 was etched in Kroll solution (1 mL HF, 3 mL HNO₃, 8 mL H₂O). The corrosion reagent of Cu and 316L are composed of 1 g FeCl₃, 3 mL HCl, 12 mL H₂O. The etched metallographic specimens were applied to optical microscopy (OM, Olympus GX7) to characterize microstructure. At the same time, the microstructure and crystal characteristics of the deposited materials were further characterized via scanning electron microscope (SEM) equipped with electron back scattering diffractometer (EBSD, Quanta 200FEG). The EBSD specimens were mechanically polished and then cross-sectional ion polished to remove surface stress. The phases and nano-microstructure detection of the interfaces were examined by transmission electron microscopy (TEM, Talos F200X, FEI, USA). Samples for the TEM characterization were firstly ground to below 50 μ m and then ion-beam milled using the Gatan 695 precision ion polishing system.

Table 2 – The chemical composition of Ti64, 316L pure and Cu wire.

Element (wt. %)	Ti6Al4V	Elements	316L	Elements	Cu
Al	6.10	Cr	16.71	Cr	≤ 0.001
V	3.92	Ni	11.62	Mn	≤ 0.001
Fe	0.12	Mn	2.16	Fe	≤ 0.001
O	0.065	Mo	2.31	Sb	≤ 0.001
C	0.06	Si	0.84	Co	≤ 0.001
Ti	Bal.	Fe	Bal.	Cu	Bal.

Table 3 – Optimized deposition parameters used in current work.

Alloys	Accelerating voltage (kV)	Beam current (mA)	Traveling speed (mm/min)	Feeding speed (mm/min)
316L on Ti64	60	35	400	1200
Cu on Ti64		25	500	1400
316L on Cu		30	350	1800

The overall distribution of micro-hardness across the interface was measured using Vickers hardness tester (HVS-50) along the building direction with a load of 10 N and a dwell time of 10 s. Furthermore, the shear strength test was performed on a universal testing machine (Instron 5569) with 0.5 mm/min loading rate. The schematic design of process for shear test, corresponding location fetched from Ti64/Cu/316L multi-materials and size for shear samples are displayed in Fig. 2. The shear strength measurements were repeated four times to verify the reliability of results. The fracture surface of shear specimens was observed by SEM to explore fracture mechanism.

3. Results and discussion

3.1. Microstructure at Ti64/316L interface

As several layers of 316L were deposited on the Ti64, the fracture occurred and the deposition process stopped immediately. The macro-morphology of Ti64/316L multi-material is shown in Fig. 3 (a). The severe fracture and delamination are observed between Ti64 and 316L. There are many longitudinal cracks on the surface of deposit. To further understand the causes for severe delamination, the microstructure of Ti64/316L interface with severe interfacial fracture and massive cracks is exhibited in Fig. 3 (b). Moreover, many cracks

distributed within a band with an approximately width of 100 μm between Ti64 and 316L, that are cold cracks with straight and smooth transgranular cracking in Fig. 3 (c). The XRD patterns of fractured surface are depicted in Fig. 4, where the Fe_2Ti (Fe, Ni) Ti , Ni_3Ti , Cr_2Ti and other IMCs are identified. The maximum micro-hardness in the vicinity of fracture interface exceed 800 HV. As generally known, Fe-Ti IMCs exhibit great brittleness [33], and the numerous Fe-Ti IMCs in Ti64/316L interface have greatly negative effect on mechanical performance of Ti64/316L multi-material.

It is believed that there are mainly two reasons for cracking even fracture in Ti64/316L interface. Firstly, the difference between Ti64 titanium alloy and 316L stainless steel for physical properties are relatively apparent, such as the linear expansion coefficient and thermal conductivity, as shown in Table 1. The deformation and thermal conduction are inconsistent during heating and cooling of molten pool at heterogeneous interface, which results in significant residual stresses at Ti64/316L interface. Secondly, the metallurgical reaction at Ti64/316L interface produce substantial hard and brittle IMCs, especially Fe-Ti IMCs, which seriously weakens the strength and plastic of material. As a result, the hard and brittle IMCs are readily subjected to stress concentration, leading to microcracks at Ti64/316L interface. In fact, the presence of cracks lead to discontinuity in deposit, which further reduces the thermal conductivity of material for subsequent deposition. This is vicious cycle during deposition

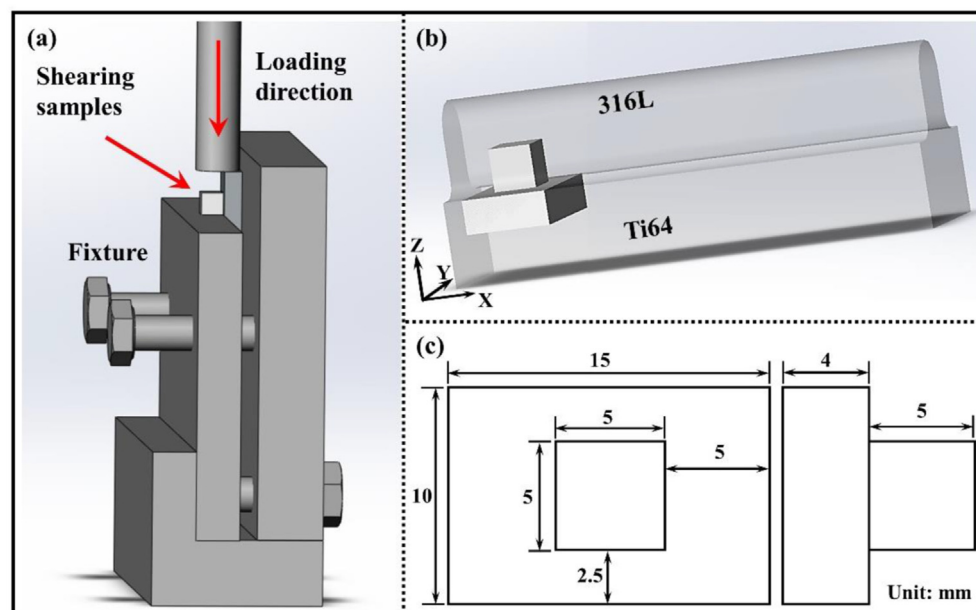


Fig. 2 – Schematic diagram of shear test, location and size: (a) the process of shear test; (b) the location of shear specimens extracted from Ti64/Cu/316L multi-materials; (c) the size of shear specimens.

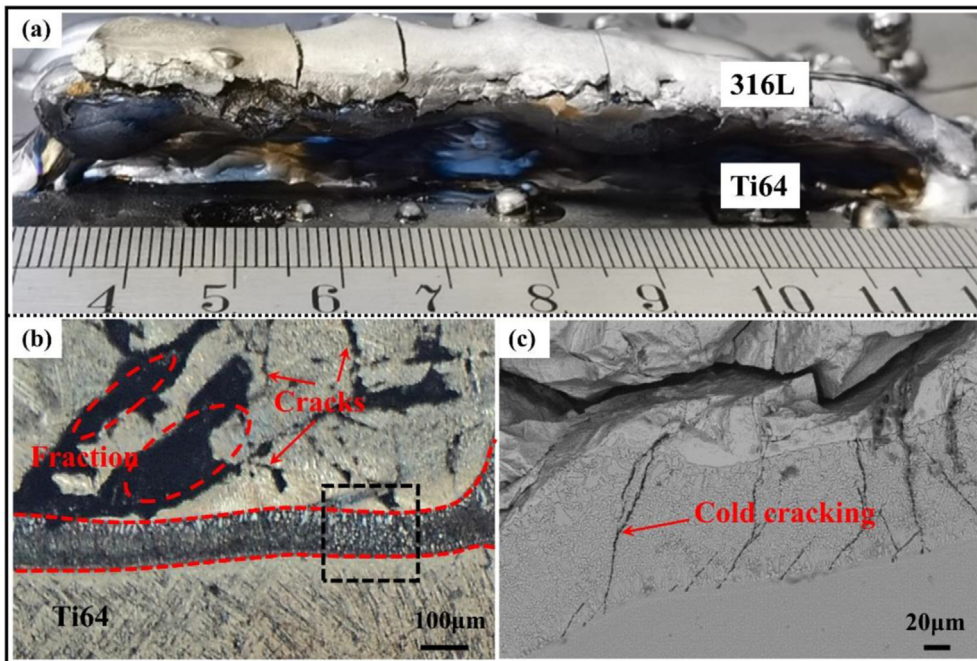


Fig. 3 – Ti64/316L multi-material prepared by EBF³ technique: (a) macro-morphology of Ti64/316L multi-material; (b) microstructure of Ti64/316L interface; (c) magnified view of black box in (b).

that the more microcracks, the more difficult for the thermal conduction, the greater the temperature difference, the more serious for cracking, until the multi-materials fracture. Therefore, this work propose energy regulation and intermediate barrier metal to reduce residual stresses and inhibit the formation of Fe–Ti IMCs. The Cu is used as the interlayer barrier metal due to its excellent ductility. The energy regulation is achieved by optimizing the deposition parameters of Cu and 316L, which reduces thermal input and diluted Ti atoms during deposition to weaken residual stress and suppress the formation of Fe–Ti IMCs. The optimized deposition parameters are listed in Table 3 and microstructures for the Ti64/Cu and Cu/316L interfaces are presented in the following sections.

3.2. Microstructure at Ti64/Cu interface

The macro-morphology of Ti64/Cu/316L multi-materials is displayed in Fig. 1 (b). Different from Fig. 3 (a), the Ti64/316L heterogeneous material with Cu interlayer have a more regular and smoother appearance without obvious defects almost. Fig. 5 presents the XRD pattern for Ti64/Cu/316L multi-materials with standard PDF. The Cu layer is relatively thin, and the space resolution of XRD equipment can not separately distinguish the two interfaces. The XRD pattern simultaneously covers five regions of Ti64, Ti64/Cu interface, Cu, Cu/316L interface and 316L. Therefore, α -Ti (Cu) and γ -Fe phases can be seen, and some IMCs such as Cu_3Ti , CuTi_2 and CuTi were recognized, which indicates that Ti64/Cu interface has become more critical as the formation of detrimental phases and has a negative impact on performance for the multi-materials.

The microstructures other than IMCs, such as (Cu) and α -Ti, could play a role in relieving stress and preventing crack propagation to a certain extent. Ahmed et al. [34] concluded that the martensitic α' -Ti could be completely attained when the cooling rate of β -Ti phase was greater than 410 K/s, and the cooling rate between 20 K/s ~ 410 K/s would form the mixed microstructures of α' -Ti and α -Ti. In fact, it is difficult to reduce the temperature of melt pool rapidly away from the substrate alone during the deposition of the material in vacuum chamber by EBF³, which would cause the remelted Ti64 to form α -Ti microstructure after solidification. In addition, the cooling rate of EBF³ is lower than that of SLM due to vacuum environment, i.e., it is not easy to form α' -Ti [35].

The microstructure of as-deposited Ti64/Cu/316L multi-materials in YOZ plane are displayed in Fig. 6. It is difficult to make the thickness of Cu interlayer uniformly distributed on the Ti64 substrate due to the high penetration and impact

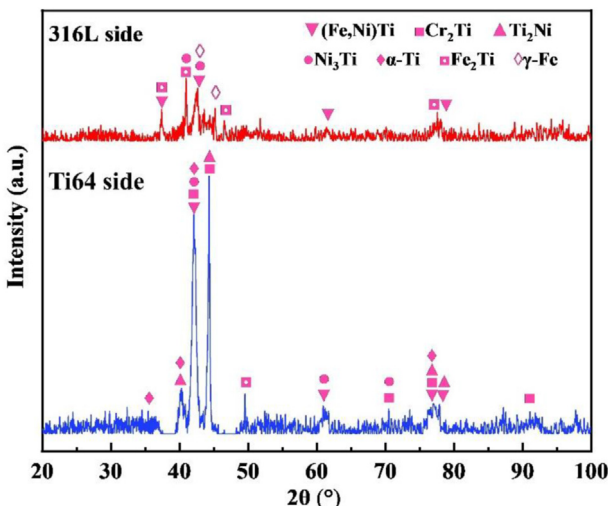


Fig. 4 – XRD pattern on both sides of fractured surface.

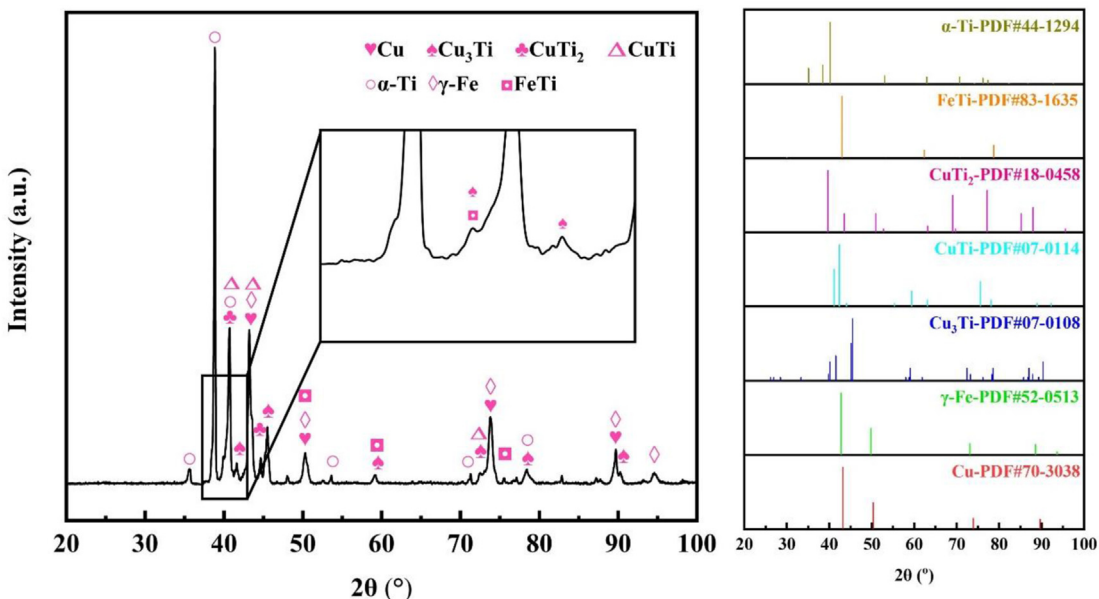


Fig. 5 – XRD pattern of Ti64/Cu/316L multi-material.

of electron beam spot, resulting in minimum and maximum thicknesses of 0.82 mm and 3.25 mm (distance between the bottom of the keyhole for Ti64 and 316L), respectively. In Fig. 6 (a), the heat affected zone (HAZ) can be seen below the Ti64/Cu interface, where many coarse grains are found and the grain size decrease with the increasing distance from the Ti64 plate. In fact, the heat is mainly dissipated through the Ti64 substrate, and the grains in the HAZ grow under the effect of thermal cycling during deposition. The heat transfer at the bottom of HAZ is fast and the grain growth is slow, which results in fine grains. There are two compound layers between Ti64 and Cu in Fig. 6 (b), namely A and B layer. The A layer is mainly composed of thin band near Ti64, lath-like and inter-lath structure, which grow epitaxially along the molten pool boundary in a columnar morphology. The B layer is defined as diffusion layer with complex Cu–Ti compounds. Above the B layer, the Cu-rich phase with dendritic morphology dominates the microstructure.

The results of EPMA quantitative analysis for the marked locations in Fig. 6 (d) and (e) are listed in Table 4. The thin band near Ti64 in A layer (point 2 in Fig. 6 (d)) possesses main composition of Cu (31.94%) and Ti (62.27%), whose atomic ratio of Ti to Cu equaled to 2. Therefore, the thin band is inferred to be Ti_2Cu by reaction between Ti and Cu atoms in molten pool. Nevertheless, Ti_2Cu is also achieved near Ti64 by $L + \alpha(Ti) \rightarrow Ti_2Cu + TiCu_2Al(\tau_1)$ [36]. The lath-like structure (point 3) exhibits equivalent content of Cu (47.61%) and Ti (47.59%), which evidently indicates as $TiCu$. In addition, the bright regions (point 5) between the lath-like $TiCu$, different from the surroundings, mainly composed of Ti (26.46%), Cu (61.27%) and Al (10.85%). According to relevant reports, when the Al content exceeds 9 at. % in the Ti–Cu–Al ternary phase diagram [37], the $TiCu_2Al(\tau_1)$ phase can be formed. However, only 6–9 at. % of Al could be observed in some bright regions (point 6). It is much lower than the stoichiometric ratio of $TiCu_2Al$ but form with the same configuration as $TiCu_2Al$ with a slight difference in lattice constant, Tey et al. called it as L₂1

[32]. It is mainly associated with the rapid solidification process of electron beam deposition, which hinder the diffusion of Al atoms to form $TiCu_2Al$ phases. Furthermore, there are few light and dark entwined structure existed in inter-lath (point 4), which maybe form via $L + Ti_2Cu \rightarrow TiCu + TiCu_2Al(\tau_1)$ peritectic reaction [36].

As displayed in Fig. 6 (e), there are dendritic structure (point 10) above B layer, which contained 87.8 at. % Cu. It can be inferred the Cu-rich solid solution with dendritic structure dissolved relatively few Ti atoms. Comparably, the more Ti diffuse to liquid in front of solid/liquid interface owing to extremely limited solubility of Ti in Cu-rich, followed solidified to form inter-dendritic regions. The constituent composed of Cu (62.13%), Fe (2.36%) and Ti (31.22%) at inter-dendrite structure (point 9) is corresponded to the $Ti_{33}Cu_{67-x}Fe_x$ on the basis of Cu–Fe–Ti ternary phase diagram [38]. The crystallographic structure of $Ti_{33}Cu_{67-x}Fe_x$ is same as that of $TiCu_2$. This is similar to Mou et al. [39] that they have observed bulk $Ti_{40}Cu_{60-x}Fe_x$ with Cu_3Ti_2 -type tetragonal structure in Ti64/Cu seam transition zone. Moreover, due to the composition contained 46.25 at. % Ti and 46.77 at. % Cu, the $TiCu$ with petal-shaped structure (point 8) dispersed in B layer is also found in Fig. 6 (e). The presence of a mixture of Cu_3Ti , $TiCu_4$ and other IMCs is speculated from the composition of other regions in B layer (point 7). However, Cu_3Ti is not exist in the Cu–Ti phase diagram. Some researches [40] thought that the Cu_3Ti phase was precipitated in a discontinuous way in Cu–Ti system.

The distribution maps of Ti, Cu and Fe in Ti64/Cu interface are presented in Fig. 7. A significant difference in composition between A and B layers due to their formation process. The areas of Ti64 beyond the effect of electron beam depend mainly on the spread of molten Cu liquid. Although the melting point of Cu (1084 °C) is lower than that of Ti64 (1725 °C), the spreading Cu liquid accumulates considerable heat, causing Ti64 to partially melt and reacted with Cu to form A layer. Simultaneously, the B layer is appeared owing to

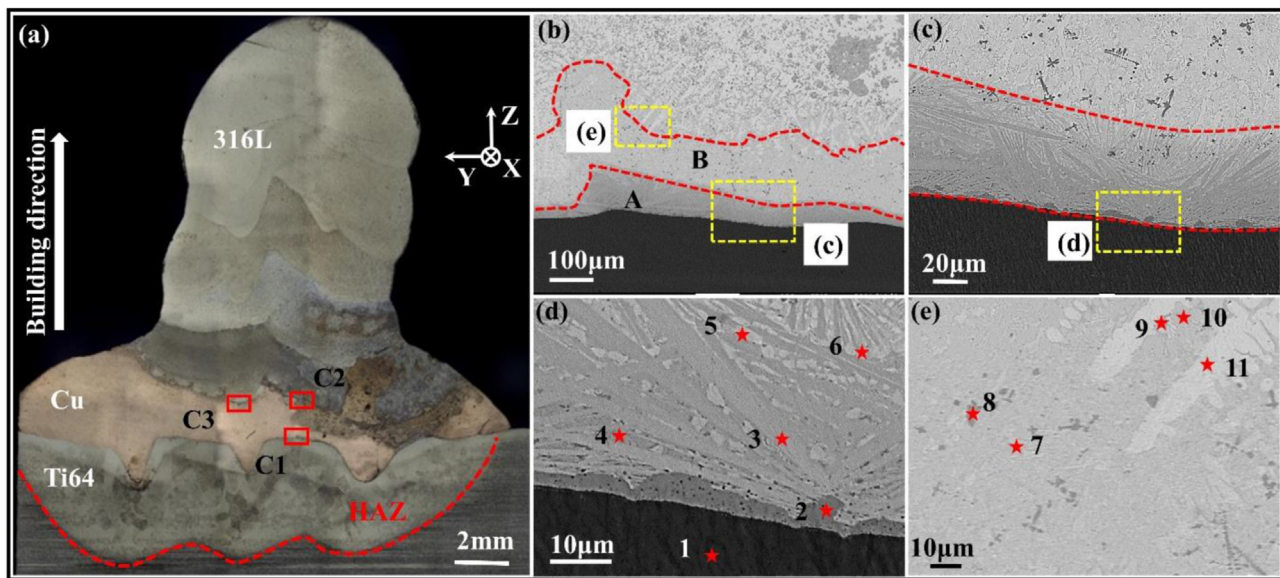


Fig. 6 – Microstructure of Ti64/Cu/316L multi-materials in YOZ plane: (a) macro-morphology of Ti64/Cu/316L multi-material; (b) microstructure of Ti64/Cu interface in C1 region; (c) enlarged image in (b); (d) enlarged image in (c); (e) enlarged image in (b).

upward diffusion of Ti atoms that combined with Cu under the effect of concentration gradient. From Fig. 6 and Table 4, the Cu content is below 50 at. %, and the Ti content reduce to 30 at. % ~50 at. % in A layer, which suggested that A layer is mainly composed of TiCu and Ti_2Cu phases. Meanwhile, the presence of fairly dispersed dendritic and petal-shaped TiCu (marked as dashed red circles) are demonstrated in Fig. 7, which is similar to chemical composition at point 8 in Fig. 6 (e). The fact is that the formed temperature of TiCu (982°C) is relatively high, which results in TiCu solidifying preferentially from the melt under the effect of elemental segregation. Along the direction of building, the Cu content increase and Ti content decrease gradually, which caused that the B layer and above are mainly consisted of Cu_3Ti and Cu-rich solid solution with dendritic structure, respectively. In addition, as the inter-diffusion of Fe and Ti atoms resulted from remelting and thermal cycling, a small amount of Fe atoms diffused into Ti64/Cu interface, which promotes the occurrence of Fe–Ti IMCs (marked as solid red circles in Fig. 7). But Cu–Ti

compounds have a major impact on the interfacial mechanical properties.

Cu-rich solid solutions offer effective relief of residual stresses through micro-deformation and play an important role in the joining of titanium steels. Accordingly, the Ti64/Cu interface is further characterized using TEM to verify the presence of Cu-rich solid solution. The region around the Cu-rich solid solution is filled with other phases (IMCs) with an atomic ratio of Fe/Ti of about 2, as shown in Fig. 8 (a) and (b). The white rectangle in Fig. 8 (c) is calibrated as Cu-rich solid solution, as shown in Fig. 8 (d), which indicated that the hard Fe–Ti IMCs particles are distributed on a rather soft matrix. The fairly dense dislocations are observed in Cu-rich solid solutions relative to other phases. The Fe–Ti IMCs particles encapsulated by Cu-rich solid solutions serve as strengthen phase by hindering dislocation motion during deformation.

The phase distribution and grains orientation are manifested in Fig. 9 at Ti64/Cu interface. The complicated Cu–Ti IMCs including $CuTi_2$ and $CuTi$ extensively distribute in

Table 4 – EPMA quantitative analysis results of marked locations in Fig. 6 (d) and Fig. 6 (e).

Spots	Elements (at. %)							Possible phases
	Ti	Cu	Fe	Cr	Ni	Al	V	
1	88.63	0.37	0.11	0	0	7.72	3.16	α -Ti + β -Ti
2	62.27	31.94	0.17	0	0	3.8	1.82	Ti_2Cu
3	47.59	47.61	0.19	0.15	0.30	1.88	2.29	TiCu
4	46.25	37.87	0.49	0.23	0.27	11.01	3.88	Ti_2Cu + TiCu + $TiCu_2Al$ (τ_1)
5	26.46	61.27	0.32	0.25	0.25	10.85	0.6	$TiCu_2Al$ (τ_1)
6	30.61	60.39	0.37	0.37	0.46	6.15	1.50	$L2_1$
7	21.83	74.9	0.79	0.65	0.69	0.59	0.55	Cu_3Ti + TiCu ₄ + TiCu ₂
8	46.25	46.77	0.47	0.33	0.29	5.05	0.84	TiCu
9	31.22	62.13	2.36	0.91	1.69	0.80	0.90	$Ti_{33}Cu_{67-x}Fe_x$
10	8.95	87.8	0.29	0.3	0.24	2.0	0.41	(Cu)

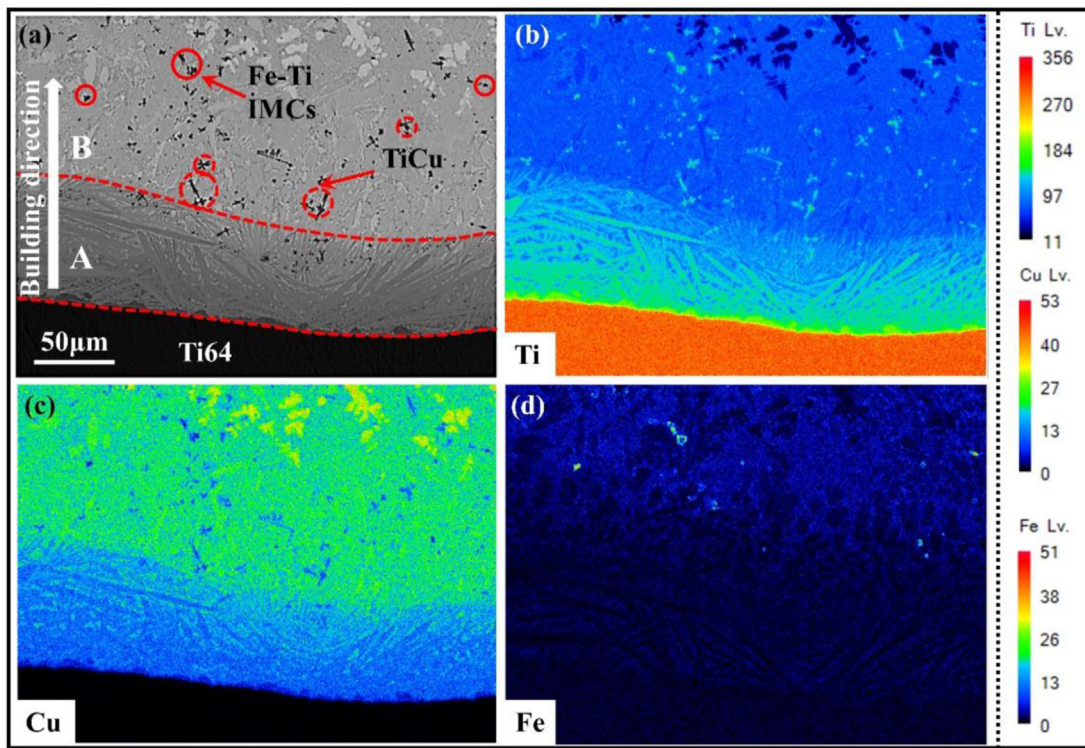


Fig. 7 – Microstructure and elemental distribution map at Ti64/Cu interface: (a) microstructure of Ti64/Cu interface; (b) Ti; (c) Cu; (d) Fe.

Figs. 9 (b), and 5.2% of FeTi also appear near the Ti64/Cu interface, which indicates that the Cu did not completely impede the interdiffusion between Fe and Ti atoms under the strong penetration of electron beam. In fact, the considerably less FeTi seem to be less sensitive to crack growth as the replacement of CuTi compared with the Ti64/316L interface, which is not conducive to crack propagation. In addition, α -Ti existed in Ti64 substrate is also observed above the interface. It is inferred that the appearance of α -Ti above the interface is caused by the convection of heterogeneous melt in the molten pool, which would have a favorable effect on the interfacial performance actually. Generally, the deformability of different phases in composite materials is inconsistent, which makes it difficult to coordinate deformation among phases and easily leads to uneven distribution of residual stresses [41]. Consequently, a large number of dislocations in the softer phase may be generated to form micro-strain and release the residual stress. This description is corroborated by the emergence of dense dislocations in the Cu-rich solid solution in Fig. 8 (c). As well, the local of α -Ti is comparatively significant compared with other phase regions, which effectively relieves stress concentration, as presented in Fig. 9 (d). Not only that, previous studies have shown that it was expected to improve the interfacial strength by increasing the content of α -Ti as this phase could inhibit crack propagation [32]. As far as known, α -Ti is believed to have similar role for the inhibition crack growth due to the small lattice difference between α -Ti and α' -Ti [42]. The critical crystallographic orientation information that affects material properties cannot be ignored, as provided in Fig. 9 (c). Obviously, the Cu–Ti IMCs above Ti64 is dominated by (001) orientation in YOZ plane, which is closely

related to the direction of maximum thermal gradient as the solid–liquid interface of the molten pool.

3.3. Microstructure at Cu/316L interface

The microstructure of Cu/316L interface are shown in Fig. 10, which present the typical microstructure of liquid phase separation. There are many spheroids near the interface. Specifically, Fe-rich spheroids (marked as solid yellow circles) are found in Cu-rich matrix, and Cu-rich ones (marked as dashed yellow circles) arose in Fe-rich matrix, which are consistent with the results of Zhang et al. [43] and Zafari et al. [44]. This structure could be explained by the existence of a metastable miscibility gap despite the fact that the liquid is infinitely miscible in the Fe–Cu system [45]. The melt undercooling formed by rapid cooling causes the liquid phase to separate into Fe-rich melt and Cu-rich melt. And then the melt solidified into spherical Fe-rich solid solution and Cu-rich solid solution at Cu/316L interface. In fact, relatively small undercooling contributes to the occurrence of liquid phase separation [46]. However, the occurrence of liquid phase separation weakens the microstructure and negatively affects the interfacial mechanical properties [46]. In addition to spheroids near the Cu/316L interface, the clusters that be made up of short rod-like structures could be also seen, which can be speculated as Fe_2Ti based on its chemical composition. Notably, considering the presence of Fe-rich bulks in the Cu-rich matrix in Fig. 10 (a), it is more like the transition region of Cu and 316L. The fusion boundary of Cu/316L are clearly identified in Fig. 10 (b) with many spheroids above the fusion boundary. The equivalent diameter of the spheroids for Fig. 10

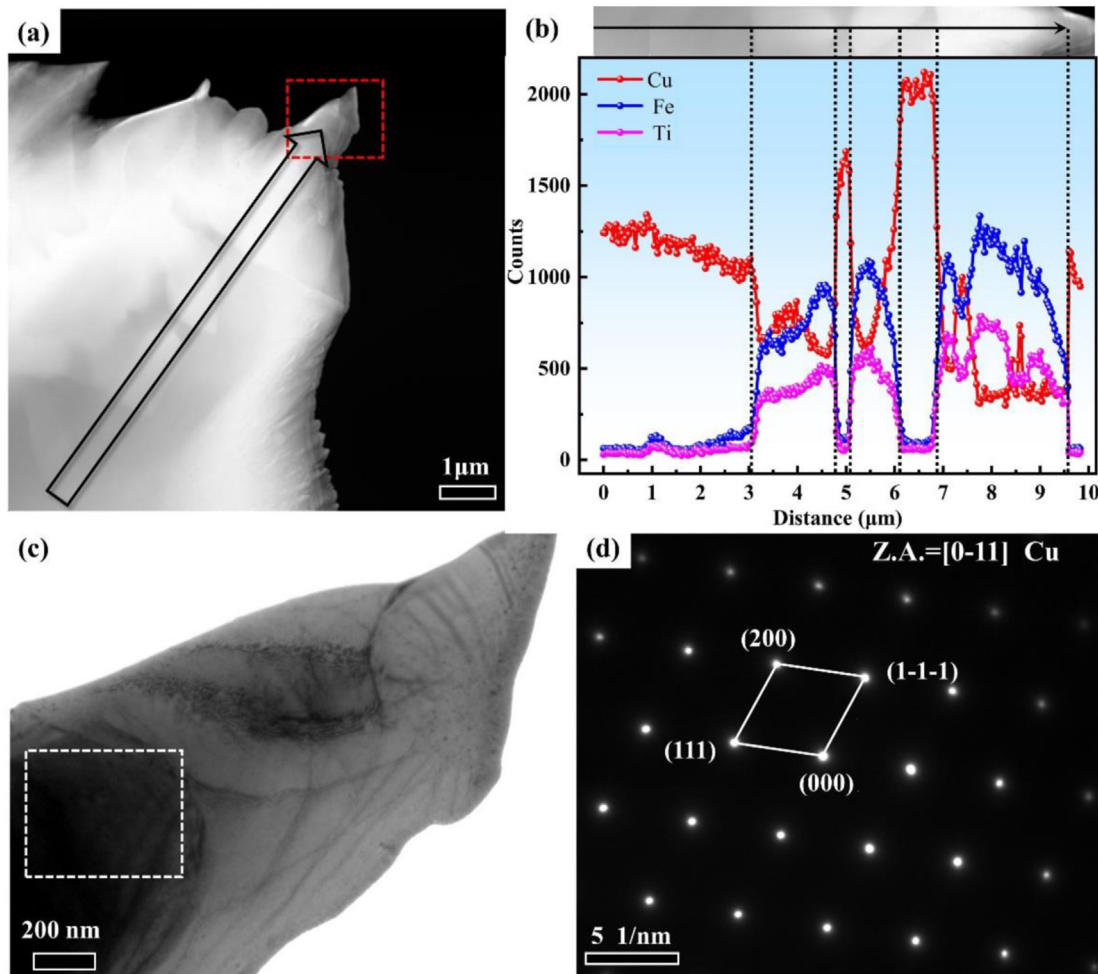


Fig. 8 – The TEM results at Ti64/Cu interface: (a) bright filed image; (b) distribution of Cu, Fe and Ti aligned with the direction of the arrow in (a); (c) magnified bright filed image in (a); (d) SAED of the white rectangle in (c).

(a) and (b) was statistically calculated by *Image Pro Plus* software, which were $14.66 \pm 4.15 \mu\text{m}$ and $5.82 \pm 2.29 \mu\text{m}$ respectively. The size of spherical solid solution depends mainly on the influence of undercooling, i.e. the radius of spheroids increase with the increase of subcooling [46], which indicates that the cooling rate of second pass is lower than that of first pass due to thermal accumulation. In contrast to Fig. 10 (a), the regions between the Cu-rich solid solution with dendritic morphology below the fusion boundary exhibit considerable amount of lamellar eutectic structures in Fig. 10 (b). This results indicate that the dendritic Cu-rich solid solution solidified, following the residual liquid phase containing the low melting point elements solidified by $\text{L} \rightarrow \text{TiCu}_4 + \text{TiCu}_2$ to formed $(\text{TiCu}_4 + \text{TiCu}_2)$ eutectic based on Cu-Ti binary phase diagram. Clearly, the larger remelting effect of electron beam would bring Ti atoms in Ti64 substrate to the upper deposited Cu layer. Part of Ti atoms dissolve in Cu-rich solid solution with dendritic morphology, some Ti atoms that discharge to interdendrite solidified with other atoms to form interdendritic compounds, and some Ti atoms would combine with Fe under the function of remelting to form Fe-Ti IMCs, as shown in Figs. 10 and 11.

As marked by the red arrows in Fig. 10 (a), some Fe/Cu-rich bands and bulks can be seen in the Cu/Fe-rich matrix, which

are caused by Marangoni convection during deposition [47]. It is believed that Marangoni convection caused a circulating flow in the molten pool, bringing the molten steel from the top to the bottom to mix with the molten copper. Then the circulating flow continued to push the mixture to the top of molten pool. The melt of copper and steel were mixed at interface, which could significantly improve the metallurgical bonding strength of interface [48].

Considering the negative impact of liquid phase separation and Fe-Ti IMCs at the interface, the Cu/316L interface for the first pass is analyzed in detail. The distribution of Ti, Cu and Fe in Cu/316L interface are shown in Fig. 11. The EPMA quantitative analysis results is listed in Table 5. This revealed more visually the distribution of Ti atoms at Cu/316L interface owing to remelting. Similar to the rod-like clusters, the ratio of Ti to Fe is close to 0.5 in some spherical Fe-rich regions, which could be speculated that the phase is Fe_2Ti . However, Ti, Cu and Fe atoms exhibit significant segregation in Fig. 11. As a result of the higher Gibbs free energy of Cu-Ti IMCs than that of Fe-Ti IMCs [39], which make the affinity of Ti to Fe greater than that to Cu, Fe preferentially combined with Ti atoms to form the hard and brittle Fe_2Ti . Therefore, under the influence of liquid phase separation, the Fe and Ti atoms are concentrated together. Since the Ti atoms have continuously been

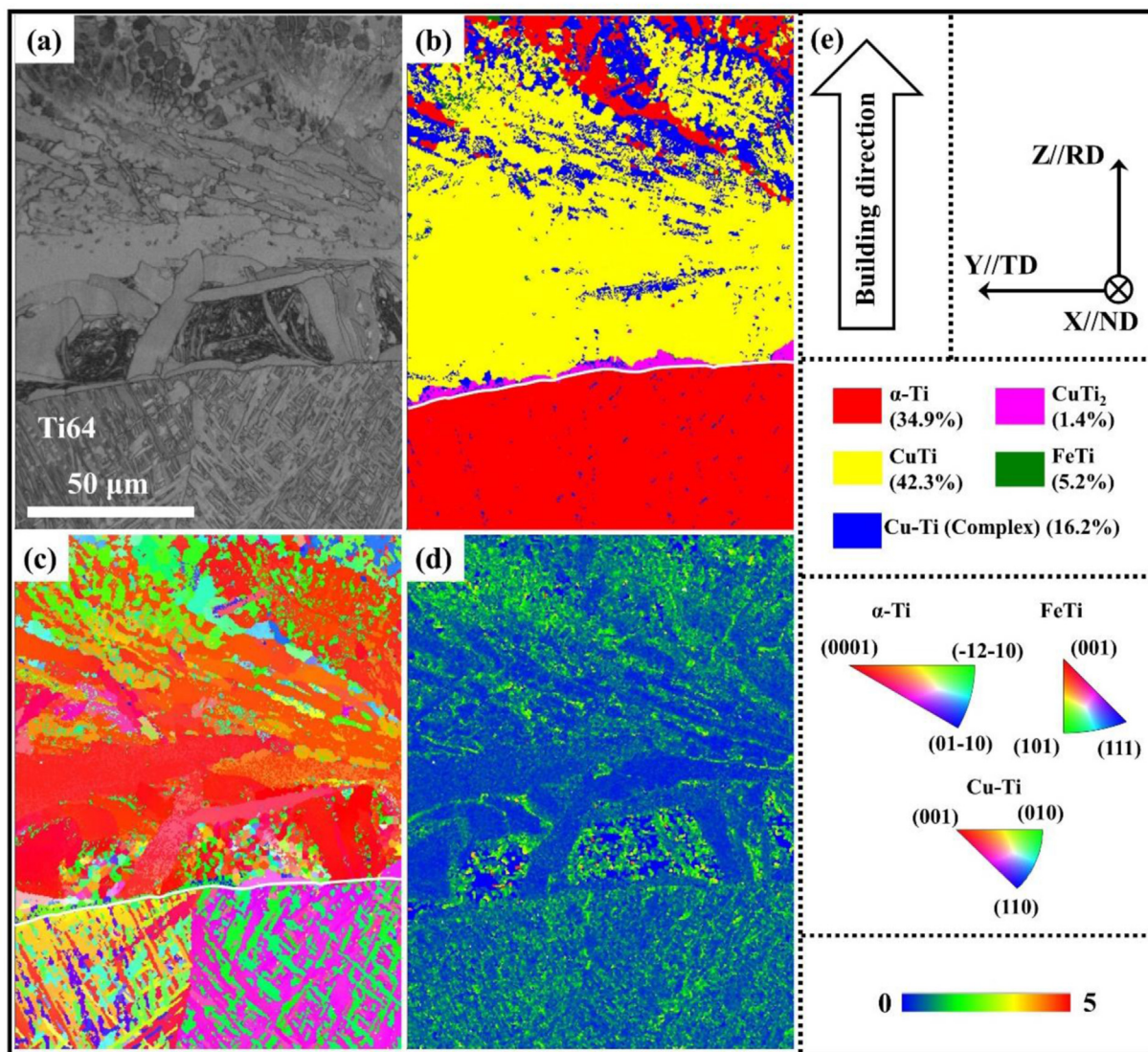


Fig. 9 – The results of EBSD analysis for Ti64/Cu/316L multi-materials at Ti64/Cu interface: (a) band contrast image; (b) phase distribution image; (c) IPF image; (d) KAM image; (e) coordinate relation, corresponding legends of phase, IPF and KAM.

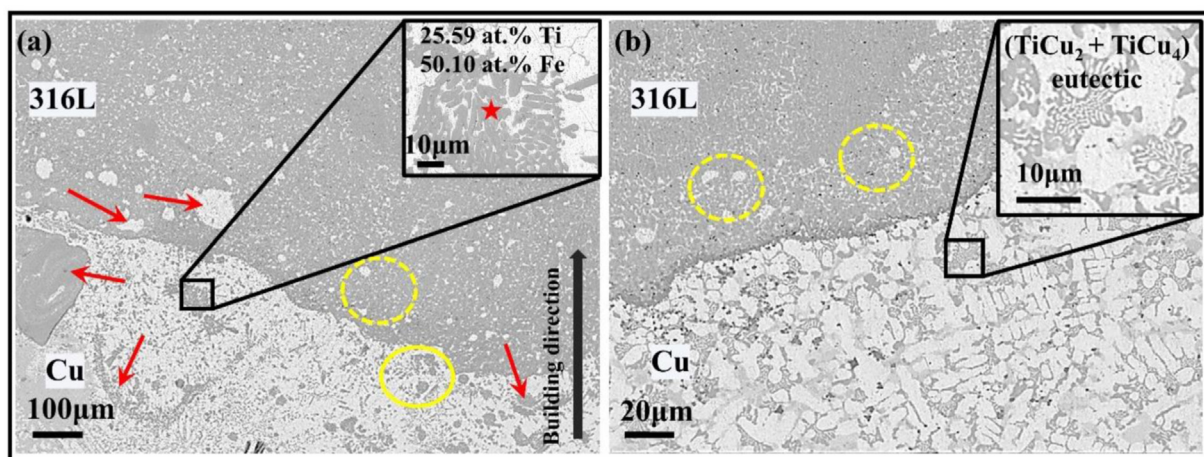


Fig. 10 – Microstructures of Cu/316L interface in Fig. 6: (a) magnified C2; (b) magnified C3.

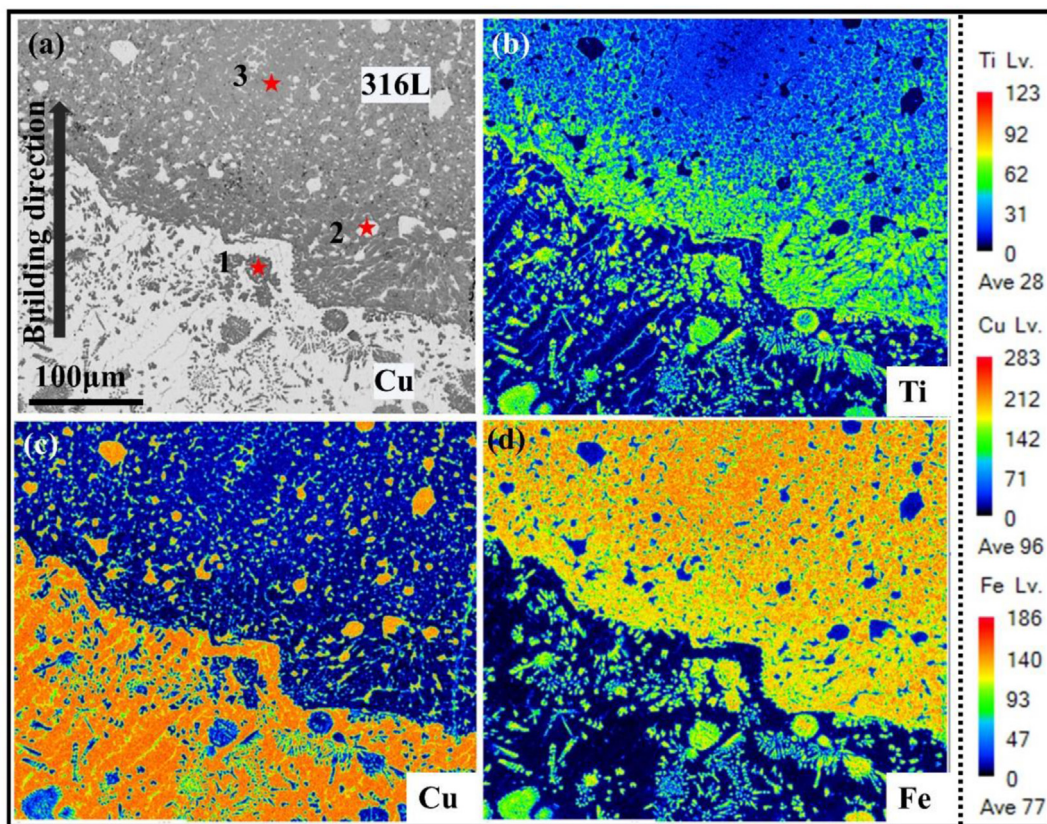


Fig. 11 – Microstructure and elemental distribution map at Cu/316L interface: (a) microstructure of Cu/316L interface; (b) Ti; (c) Cu; (d) Fe.

diluted during the subsequent deposition of 316L, resulting in fewer Ti atoms with the increased distance from the interface. It is noted that the Cu solubility in the Fe-rich phase increased in proportion to the Ti content, so that the formed Ti–Fe compounds could dissolve 35 at. % of Cu atoms [38], which is the reason for the atomic content of Cu at point 1 and 3 exceeded 10% in Fig. 11. In addition, it is obvious that the growth direction of dendritic Cu-rich solid solution is perpendicular to the Cu/316L interface, and Ti atoms are segregated at interdendrite in Fig. 11 (b) and (c).

Generally, the purpose of isolating Ti64 and 316L stainless steel with Cu as the interlayer is to utilize the excellent plastic deformation ability of Cu-rich solid solution to alleviate the residual stresses caused by dissimilar alloy characteristics mismatch. Thus, it is expected that the Cu-rich solid solution in Cu layer may be deformed to some extent. The phase distribution and KAM image in Cu interlayer are shown in Fig. 12, which is dominated by Cu-rich solid solution and γ -Fe. Compared with the KAM at Ti64/Cu interface, the KAM in Cu

interlayer is significantly higher, indicating that the Cu-rich solid solution has indeed played a role in releasing stress. Nevertheless, it is observed that the KAM region with high values is concentrated on γ -Fe in Fig. 12 (c). Studies have shown that in the manufacturing process of 316L and CuSn10 dissimilar alloys, high residual stress was easily conducted in 316L with lower thermal expansion than CuSn10 [49].

3.4. Microstructure evolution of Ti64/Cu/316L multi-materials

Assuming that the process of wire feeding into the molten pool is a liquid bridge transition, we could describe schematic diagrams of microstructure evolution of Ti64/Cu and Cu/316L interfaces during solidification based on the analysis results of microstructure and phase distribution characteristics at each interface. As quite complex IMCs exist at the Ti64/Cu interface, it is necessary to resort to the Al–Cu–Ti isothermal section ternary phase diagram at 850 °C summarized by V.

Table 5 – EPMA quantitative analysis results of marked locations in Fig. 11 (a).

Spot	Elements (at. %)							Possible phases
	Ti	Cu	Fe	Cr	Ni	Al	V	
1	21.86	10.26	46.46	13.17	6.46	0.65	1.14	Fe ₂ Ti
2	3.09	86.2	2.7	1.03	5.26	1.66	0.06	(Cu)
3	7.14	13.88	52.66	16.42	8.98	0.52	0.4	γ -Fe

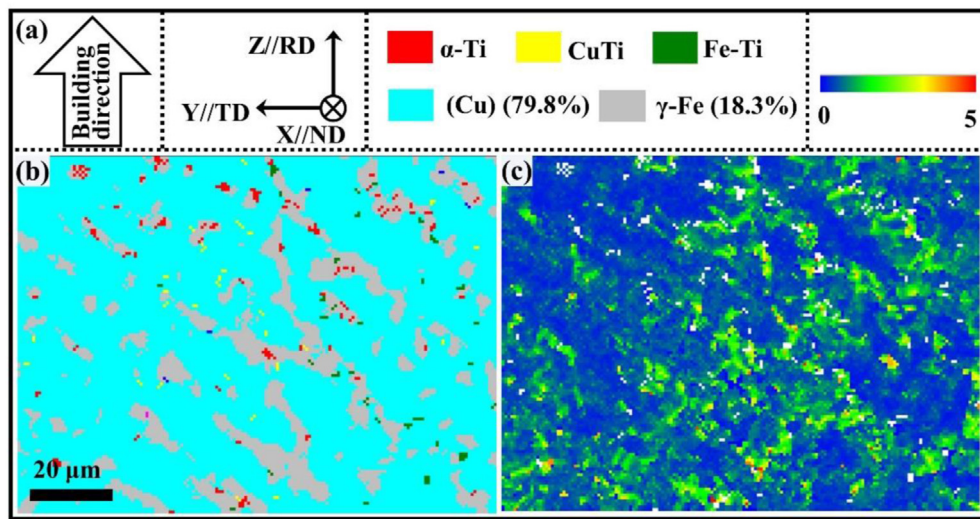


Fig. 12 – The results of EBSD analysis at Cu interlayer: (a) coordinate relation, corresponding legends of phase and KAM; (b) phase distribution image; (c) KAM image.

Raghavan [37] as a means to understand more intuitively the microstructural evolution at the Ti64/Cu interface. The shift in composition during solidification at the Ti64/Cu interface is similar to the direction of the red dashed line, as shown in Fig. 13. Wherein, Ti and Cu atoms decrease and increase, respectively, with the advancement of solidification interface, which is consistent with the distribution of that along the building direction in Fig. 7. Moreover, the phases or IMCs formed by compositional changes in the direction of the red dashed line are almost observed at the Ti64/Cu interface. Whereas the phases that not presented may be due to the non-equilibrium solidification of additive manufacturing. It should be emphasized that the liquid-to-solid phase transition process is not addressed in Fig. 13. Therefore, the detailed formation and solidification of molten pool at interfaces are depicted in Fig. 14, which can be summarized into four characteristic stages.

- (1) First, the electron beam heat source acts on the Ti64 substrate. In the conditions of high energy density heat source, the Ti64 substrate and the Cu wire stably fed into the molten pool are melted rapidly, as shown in Fig. 14 (a). With the establishment and stability of molten pool, the melt is mainly composed of Ti, Cu, Al and V atoms. As a result of strong convection, electron beam impact and atomic concentration gradient in the molten pool, the Ti atoms at the bottom of molten pool diffuse upward, and the Cu atoms at the top of molten pool rapidly diffuse downward, but the overall distributions of Ti and Cu atoms are higher at bottom and top, respectively. At the same time, Ti64 melt circulates upward by Marangoni force.
- (2) The second stage is presented in Fig. 14 (b), with the workbench moving, the effect of electron beam on the previous position is weakened, and the molten pool start to solidify. In a vacuum environment, the heat of molten pool dissipated through the Ti64 substrate. Considering the high transition temperature of α -Ti

($< 1490^\circ\text{C}$), the Ti64 melt at the bottom of the molten pool that no time to diffuse would solidified into α -Ti. As the temperature continuously decrease, the boundary of solid–liquid contribute to nucleation, and the thin band of Ti_2Cu closed to Ti64 is formed by reaction $\text{L} + \alpha(\text{Ti}) \rightarrow \text{Ti}_2\text{Cu} + \text{TiCu}_2\text{Al}(\tau_1)$ [36]. Moreover, Ti and Cu also would be synthesized into Ti_2Cu and lath-like TiCu below 982°C due to the enthalpy of formation are relatively low. The more $\text{TiCu}_2\text{Al}(\tau_1)$ appear between lath-like TiCu and Ti_2Cu through $\text{L} + \text{Ti}_2\text{Cu} \rightarrow \text{TiCu} + \text{TiCu}_2\text{Al}(\tau_1)$ [36] according to the Al–Ti–Cu ternary phase diagram. Therefore, $\text{TiCu} + \text{TiCu}_2\text{Al}(\tau_1)$ peritectic structure may be observed between lath-like TiCu , as shown in Fig. 6 (d). But the cooling rate is fast, and the peritectic reaction could not be completely completed.

- (3) The third stage is displayed in Fig. 14 (c), not only the temperature of molten pool decrease, but also the concentration of Ti atoms reduce, which led to successive appearance of Cu–Ti complex IMCs, such as TiCu_2 , TiCu_3 and TiCu_4 etc. When Ti atoms are exhausted, Cu atoms dominate the molten pool, and dendritic Cu-rich solid solutions could be formed along the direction of heat dissipation. Subsequently, the Cu-rich dendrites react with the residual liquid phase located in inter-dendrites to form eutectic structure through reaction $\text{L} \rightarrow \text{TiCu}_4 + \text{TiCu}_2$, as shown in Fig. 10 (b). Notably, the fact is that the growth direction of grains is closely related to the heat dissipation direction. Since the Ti64 substrate is almost the only direction of heat dissipation, the Cu-rich solid solution grow toward the center of melt pool in the form of dendrites along the direction opposite to the heat dissipation, as shown in Fig. 11. Finally, the molten pool with substantial Cu atoms solidify and form Ti64/Cu interface.
- (4) The last stage is depicted in Fig. 14 (d), when 316L is deposited on solidified Cu, the Cu-rich regions are

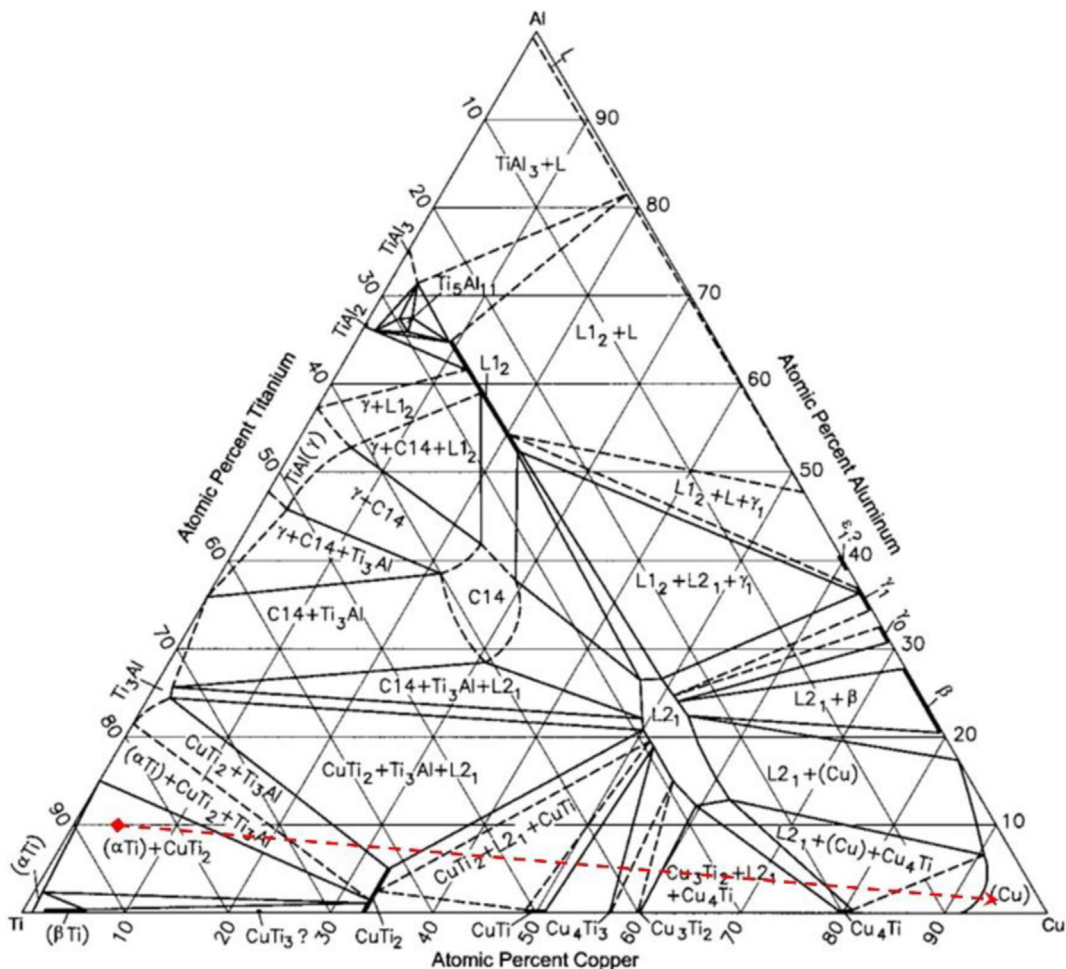


Fig. 13 – Al–Cu–Ti isothermal section at 850 °C [37].

partially remelted under the effect of electron beams, but the miscibility of Fe and Cu atoms is relatively poor. Under the condition of rapid cooling, the liquid phase separation leading to the appearance of spheres at interface occurred due to the metastable miscibility gap of Fe–Cu system. In addition, Fe atoms in molten pool are discharged to the inter-dendritic melt during the solidification of Cu-rich dendrites and combine with Ti and Cu atoms to form $Ti_{33}Cu_{67-x}Fe_x$, which have same crystallographic structure with $TiCu_2$ [38]. The heat input during the deposition have a heat treatment effect on the deposited, which results in some Cu–Ti IMCs might precipitate $TiCu_3$ in the form of discontinuous precipitation [40]. Since the diffusion coefficient of Fe atoms in Cu is extremely low, which hinder the diffusion of Fe atoms. However, some Fe atoms would be pushed to Ti64/Cu interface in view of the impact effect of electron beam, leading to the formation of Fe–Ti IMCs. And the diffusion of Ti atoms to the Cu/316L interface also result in Fe–Ti IMCs. Along the building direction, the Ti atoms decrease and the final microstructure mainly consists of austenite in 316L.

3.5. Mechanical properties and fracture analysis of multi-materials

The micro-hardness distribution of Ti64/Cu/316L multi-materials is shown in Fig. 15. Due to the coarse grains in HAZ, the micro-hardness of Ti64 side near the interface present a decrease trend. The micro-hardness reaches a maximum of 490 HV as the formation of $CuTi_2$ and $CuTi$ in the Ti64/Cu transition region, which is similar to the previous research results [50]. As a result of presence of α -Ti, Cu-rich solid solution and complex Cu–Ti IMCs, micro-hardness would be as low as 277 HV in Ti64/Cu transition region. Besides, although Ti diffuse to the Cu/316L interface under the effect of remelting and mixing to form a small amount of Fe–Ti IMCs, the micro-hardness is not high and only about 376HV, which is attributed to the surrounding environment of Cu-rich and Fe-rich solid solution matrix. As the height of as-deposited increase, Ti atoms decrease to low level, and the microstructure is mainly austenite stainless, so that the micro-hardness further reduce to 180 HV.

Considering that the complex and substantial Cu–Ti IMCs at Ti64/Cu interface have an undesirable function on bonding strength for Ti64/Cu/316L multi-materials. Therefore, the

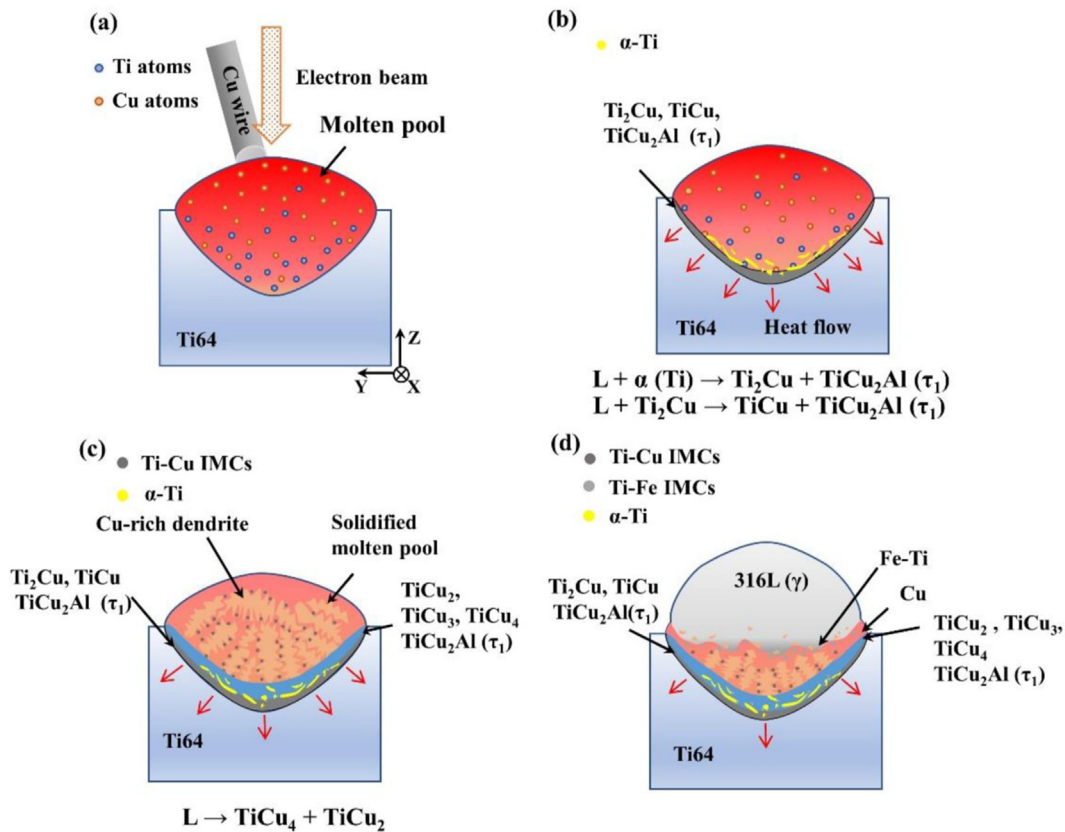


Fig. 14 – Schematic diagram of microstructure evolution during interfaces solidification: (a) first stage; (b) second stage; (c) third stage; (d) forth stage.

shear test is performed on the Ti64/Cu interface to examine the extent of damage to the material. In fact, the uniaxial tensile tests loaded along the building direction have been carried out prior to the shear tests. The Ti64/Cu and Cu/316L interfaces are contained within the gauge length of tensile samples. As expected, the tensile strength and plasticity were unsatisfactory (151.4 MPa and 2.48%) and all of the failure locations occurred at the Ti64/Cu interface.

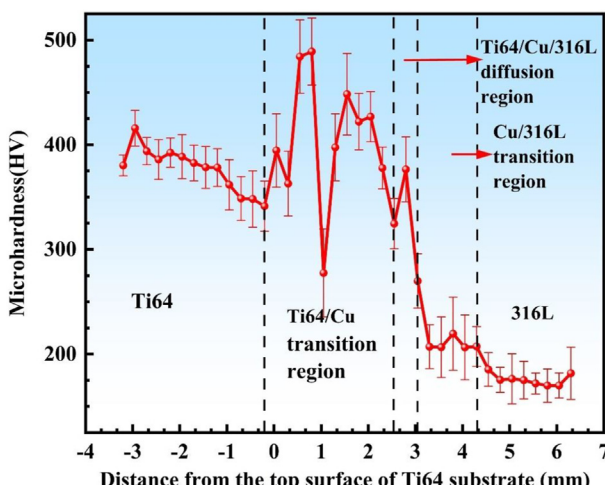


Fig. 15 – Micro-hardness distribution of Ti64/Cu/316L multi-materials.

Consequently, the Ti64/Cu interface become a critical interface prone to failure relative to the Cu/316L interface. As a result of the shear tests, the Ti64/Cu interface exhibits relatively excellent shear resistance with a shear strength of 196.5 ± 2.2 MPa, which is slight higher than that of partial titanium/steel joint prepared by infrared brazing (176 MPa [51]), friction stir welding (> 178 MPa [52]), diffusion bonding (105.2 MPa [53], 158 MPa [54]), etc. The schematic diagram of shearing process and the fracture morphology of both sides are displayed in Fig. 16. Obviously, the fracture surfaces exhibit relatively rough morphology. Fig. 16 (b) shows many microcracks, cleavage steps and river patterns on the fracture surface of Ti64 side. The side of Ti64 presents a typical brittle fracture feature. In Fig. 16 (c), the tearing edge appeared on the Cu side, forming pits similar to the dimple. There are also microcracks and small pores at the bottom of pits, which indicates that the Ti64/Cu interface possesses great brittleness causing some IMCs peeled off. However, the presence of Cu-rich solid solution moderate the shear strength.

Two reasons for the good shear strength of Ti64/Cu interface. First, the Ti64 substrate is subjected to several preheat before feeding wire and experienced thermal cycles during EBF³, which is benefit to the formation of keyhole mode [55], as shown in Fig. 16 (a). Subsequently, the Cu melt is embedded in the Ti64 substrate and then solidify, forming molten pool boundary similar to a pin shape, which could play a role in pinning reinforcement. This is consistent with

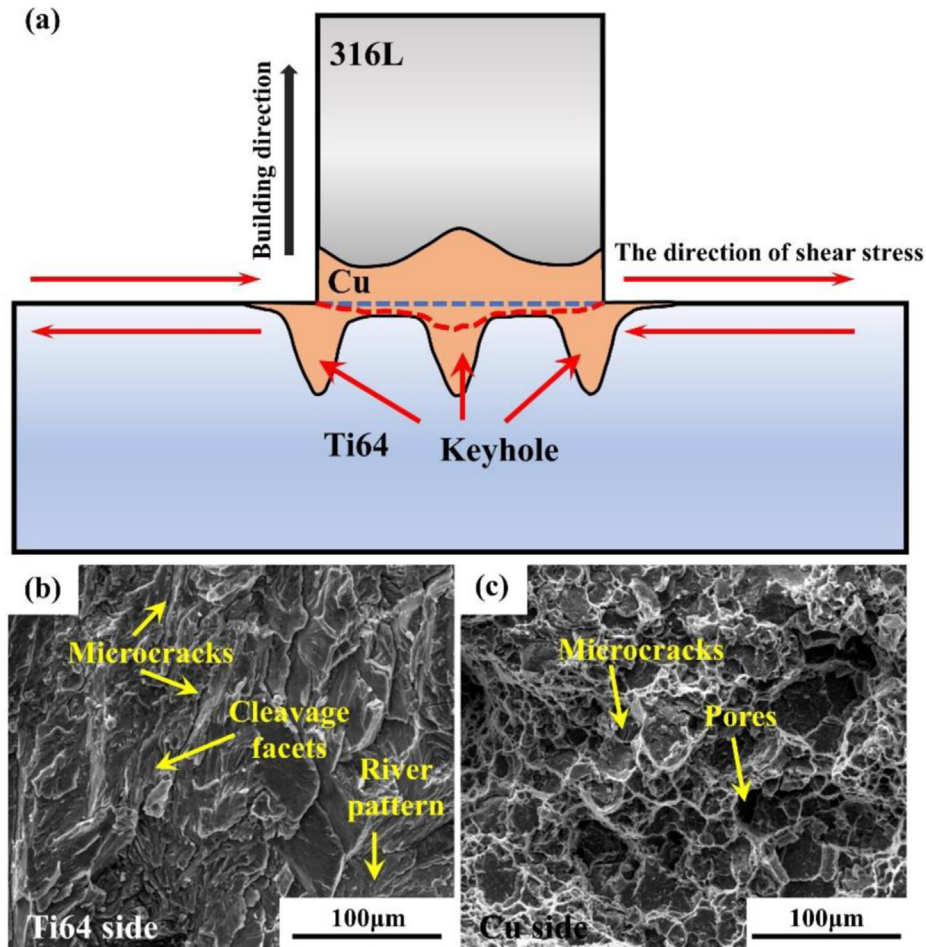


Fig. 16 – Shearing process and fracture microstructure: (a) schematic diagram of shearing process; (b) fracture morphology of Ti64 side; (c) fracture morphology of Cu side.

Chao et al. [56] that the tip of keyhole could reinforce bonding strength between Cu layers and solidified Ti layers. Secondly, although the hard and brittle Cu-Ti IMCs continuously distribute in the A and B layers deteriorated the shear of multi-materials, as shown in Fig. 6 (b), there are α -Ti and Cu-rich solid solution with good plasticity at Ti64/Cu interface, which could accommodate large shear strain. Meanwhile, the Cu-Ti IMCs located between dendritic Cu-rich solid solution present hardness and brittleness, which obstructs deformation of Ti64/Cu interface. The dendritic Cu-rich solid solution and interdendritic Cu-Ti IMCs achieve a synergistic strengthening ability as the shear test is implemented. In addition, the fracture surface depressed toward Ti64 is observed and the schematic boundary of fracture surface (marked as red dashed line) is displayed in Fig. 16 (a). It can be interpreted that under the effect of shear stresses, the expanded cracks deflected when it encountered α -Ti and Cu-rich solid solution with interdendritic Cu-Ti IMCs, and turned to the Cu-Ti IMCs regions for extension and then fracture. As a result, the fracture occurred in the regions with substantial hard and brittle IMCs, so that the surfaces of shear fracture were uneven and recessed toward the Ti64 side.

4. Conclusions

In this work, the Ti64/316L multi-materials that fabricated by EBF³ technique present substantial defects, which is impossible to develop into industrial applications. Nevertheless, owing to physical characteristics of Cu, it is potential that Cu as the interlayer between Ti64 and 316L would reduce even avoid the appearance of defects. Therefore, Ti64/Cu/316L multi-materials manufactured by EBF³-technique are investigated in detail, especially microstructure and mechanical properties for Ti64/Cu and Cu/316L interfaces. The following main conclusions can be drawn.

- (1) The direct deposition of 316L on Ti64 substrate using EBF³ causes many cracks and delamination at Ti64/316L interface due to the great differences in physical behavior between Ti64 and 316L as well as the emergence of numerous hard and brittle Fe-Ti IMCs, which seriously damage the structural continuity of multi-material.
- (2) With the addition of Cu interlayer, there is formed complex Cu-Ti IMCs at Ti64/Cu interface, such as Ti_2Cu , $TiCu$, $TiCu_2Al(\tau_1)$, Cu_3Ti , and $TiCu_2$, etc. The α -Ti

and dendritic Cu-rich solid solution with excellent plasticity are also observed, which effectively relieve the residual stresses concentration. Spherical Fe-rich and Cu-rich solid solutions exist at Cu/316L interface, but the Fe-rich solid solution contain some Fe–Ti IMCs that resulted from the diffusion of Ti atoms. A little Fe–Ti are also found near Ti64/Cu interface due to the impact of electron beam. The Cu–Ti IMCs have less negative effect on mechanical property for Ti64/Cu/316L multi-materials relative to Fe–Ti IMCs.

- (3) The maximum micro-hardness of Ti64/Cu/316L multi-materials is located at Ti64/Cu interface with 490 HV in view of the existence of CuTi₂ and CuTi. The micro-hardness of Cu/316L interface that surrounding of Cu-rich and Fe-rich solid solution matrix is not high. The Ti64/Cu interface exhibits superior shear strength with 196.5 ± 2.2 MPa, which is attributed to the reinforcement for the tip of keyhole mode molten pool, as well as synergy between Cu-rich solid solution and interdendritic Cu–Ti IMCs.

The original intention of this research is to use soft Cu to relieve stresses concentration and replace the extremely hard and brittle Fe–Ti IMCs with the formed Cu–Ti IMCs. Although the Ti64/Cu/316L multi-materials is triumphantly deposited by EBF³ in this work, the mechanical property is relatively ordinary compared with other processes. In particular, the existence of complex Cu–Ti IMCs seriously weaken the plasticity of multi-materials. Therefore, our future works will focus on thermodynamically analyzing the feasibility of eliminating IMCs and designing compositional pathway along the direction from Ti64 to 316L through binary or ternary phase diagrams to avoid the emergence of deleterious phase, which will have great guiding significance for improving the mechanical property of multi-materials.

CRediT authorship contribution statement

Guoqiang Zhu: Conceptualization, Data curation, Formal analysis, Writing – original draft. **Liang Wang:** Formal analysis, Project administration, Funding acquisition. **Binbin Wang:** Conceptualization, Formal analysis. **Binqiang Li:** Formal analysis, Writing – review & editing. **Junbo Zhao:** Investigation. **Bao Ding:** Investigation. **Ran Cui:** Writing – review & editing. **Botao Jiang:** Investigation. **Chunzhi Zhao:** Investigation, Validation. **Baoxian Su:** Writing – review & editing. **Liangshun Luo:** Conceptualization. **Ruirun Chen:** Conceptualization. **Yanqing Su:** Conceptualization, Project administration. **Jingjie Guo:** Supervision.

Declaration of Competing Interest

The authors declare that they have no known competing financial interests or personal relationships that could have appeared to influence the work reported in this paper.

Acknowledgments

This work was supported by the National Key Research and Development Program of China (Grant no. 2022YFF0609000), National Natural Science Foundation of China (Grant no. 52171034, and 52101037).

REFERENCES

- [1] Akman E, Demir A, Canel T, Sınmazçelik T. Laser welding of Ti6Al4V titanium alloys. *J Mater Process Technol* 2009;209:3705–13. <https://doi.org/10.1016/j.jmatprotec.2008.08.026>.
- [2] Thomas G, Pant B, Ganesan R, Ramachandra V, Vasudevan R. Effect of hot working temperature on the weldability of Ti-6Al-4V alloy. *Indian Weld J* 1992;25:153–8.
- [3] Jiang B, Wang L, Yan H, Zhu G, Teng J, Wang B, et al. Hydrogen-induced modification of the interface between matrix and ceramic phase of (TiB + TiC)/Ti-6Al-4V. *Compos Commun* 2023;37:101434. <https://doi.org/10.1016/j.coco.2022.101434>.
- [4] Szymlek K. Review of titanium and steel welding methods. *Adv Mater Sci* 2008;8. <https://doi.org/10.2478/v10077-008-0023-4>.
- [5] Yefei G, Takuya T, Kazuhiro N. Dissimilar welding of titanium alloys to steels. 2012.
- [6] Bhavar V, Kattire P, Thakare S, patil S, Singh R. A review on functionally gradient materials (FGMs) and their applications. *IOP Conf Ser Mater Sci Eng* 2017;229:012021. <https://doi.org/10.1088/1757-899X/229/1/012021>.
- [7] Ghanavati R, Naffakh-Moosavy H. Additive manufacturing of functionally graded metallic materials: a review of experimental and numerical studies. *J Mater Res Technol* 2021;13:1628–64. <https://doi.org/10.1016/j.jmrt.2021.05.022>.
- [8] Guo S, Zhou Q, Kong J, Peng Y, Xiang Y, Luo T, et al. Effect of beam offset on the characteristics of copper/304stainless steel electron beam welding. *Vacuum* 2016;128:205–12. <https://doi.org/10.1016/j.vacuum.2016.03.034>.
- [9] Zhang Y, Zhou J, Sun D, Gu X Nd. YAG laser welding of dissimilar metals of titanium alloy to stainless steel without filler metal based on a hybrid connection mechanism. *J Mater Res Technol* 2020;9:1662–72. <https://doi.org/10.1016/j.jmrt.2019.12.001>.
- [10] Ghosh M, Chatterjee S. Characterization of transition joints of commercially pure titanium to 304 stainless steel. *Mater Char* 2002;48:393–9. [https://doi.org/10.1016/S1044-5803\(02\)00306-6](https://doi.org/10.1016/S1044-5803(02)00306-6).
- [11] Ananthakumar K, Kumaran S. Plasma assisted diffusion joining of CP-titanium-304L stainless steel: attributes of temperature and time. *Mater Today Proc* 2020;33:3174–6. <https://doi.org/10.1016/j.matpr.2020.04.099>.
- [12] Kahraman N, Gülenç B, Findik F. Joining of titanium/stainless steel by explosive welding and effect on interface. *J Mater Process Technol* 2005;169:127–33. <https://doi.org/10.1016/j.jmatprotec.2005.06.045>.
- [13] Meshram SD, Mohandas T, Reddy GM. Friction welding of dissimilar pure metals. *J Mater Process Technol* 2007;184:330–7. <https://doi.org/10.1016/j.jmatprotec.2006.11.123>.
- [14] Soltni Tashi R, Akbari Mousavi SAA, Mazar Atabaki M. Diffusion brazing of Ti-6Al-4V and austenitic stainless steel using silver-based interlayer. *Mater Des* 1980-2015 2014;54:161–7. <https://doi.org/10.1016/j.matdes.2013.07.103>.

- [15] Hofmann DC, Roberts S, Otis R, Kolodziejska J, Dillon RP, Suh J, et al. Developing gradient metal alloys through radial deposition additive manufacturing. *Sci Rep* 2014;4:5357. <https://doi.org/10.1038/srep05357>.
- [16] Chen X, Han J, Wang J, Cai Y, Zhang G, Lu L, et al. A functionally graded material from TC4 to 316L stainless steel fabricated by double-wire + arc additive manufacturing. *Mater Lett* 2021;300:130141. <https://doi.org/10.1016/j.matlet.2021.130141>.
- [17] Rashkovets M, Mazzarisi M, Nikulina AA, Casalino G. Analysis of laser direct stainless steel powder deposition on Ti6Al4V substrate. *Mater Lett* 2020;274:128064. <https://doi.org/10.1016/j.matlet.2020.128064>.
- [18] Su YY, Wang ZF, Xie JC, Xu G, Xing F, Luo KY, et al. Microstructures and mechanical properties of laser melting deposited Ti6Al4V/316L functional gradient materials. *Mater Sci Eng, A* 2021;817:141355. <https://doi.org/10.1016/j.msea.2021.141355>.
- [19] Kundu S, Ghosh M, Laik A, Bhanumurthy K, Kale GB, Chatterjee S. Diffusion bonding of commercially pure titanium to 304 stainless steel using copper interlayer. *Mater Sci Eng, A* 2005;407:154–60. <https://doi.org/10.1016/j.msea.2005.07.010>.
- [20] Tomashchuk I, Sallamand P, Andrzejewski H, Grevey D. The formation of intermetallics in dissimilar Ti6Al4V/copper/AISI 316 L electron beam and Nd:YAG laser joints. *Intermetallics* 2011;19:1466–73. <https://doi.org/10.1016/j.intermet.2011.05.016>.
- [21] Tomashchuk I, Sallamand P, Belyavina N, Piloz M. Evolution of microstructures and mechanical properties during dissimilar electron beam welding of titanium alloy to stainless steel via copper interlayer. *Mater Sci Eng, A* 2013;585:114–22. <https://doi.org/10.1016/j.msea.2013.07.050>.
- [22] Chattopadhyay A, Muvvala G, Sarkar S, Racherla V, Nath AK. Mitigation of cracks in laser welding of titanium and stainless steel by in-situ nickel interlayer deposition. *J Mater Process Technol* 2022;300:117403. <https://doi.org/10.1016/j.jmatprotec.2021.117403>.
- [23] Mannucci A, Tomashchuk I, Mathieu A, Bolot R, Cicala E, Lafaye S, et al. Use of pure vanadium and niobium/copper inserts for laser welding of titanium to stainless steel. *J Adv Join Process* 2020;1:100022. <https://doi.org/10.1016/j.jajp.2020.100022>.
- [24] Tomashchuk I, Grevey D, Sallamand P. Dissimilar laser welding of AISI 316L stainless steel to Ti6-Al4–6V alloy via pure vanadium interlayer. *Mater Sci Eng, A* 2015;622:37–45. <https://doi.org/10.1016/j.msea.2014.10.084>.
- [25] Balasubramanian M. Characterization of diffusion-bonded titanium alloy and 304 stainless steel with Ag as an interlayer. *Int J Adv Manuf Technol* 2016;82:153–62. <https://doi.org/10.1007/s00170-015-7376-8>.
- [26] Kundu S, Chatterjee S. Evolution of interface microstructure and mechanical properties of titanium/304 stainless steel diffusion bonded joint using Nb interlayer. *ISIJ Int* 2010;50:1460–5. <https://doi.org/10.2355/isijinternational.50.1460>.
- [27] Taufiqurrahman I, Lenggo Ginta T, Mustapha M. The effect of holding time on dissimilar resistance spot welding of stainless steel 316L and Ti6Al4V titanium alloy with aluminum interlayer. *Mater Today Proc* 2021;46:1563–8. <https://doi.org/10.1016/j.matpr.2020.07.237>.
- [28] Meng W, Zhang W, Zhang W, Yin X, Guo L, Cui B. Additive fabrication of 316L/Inconel625/Ti6Al4V functionally graded materials by laser synchronous preheating. *Int J Adv Manuf Technol* 2019;104:2525–38. <https://doi.org/10.1007/s00170-019-04061-x>.
- [29] Reichardt A, Dillon RP, Borgonia JP, Shapiro AA, McEnerney BW, Momose T, et al. Development and characterization of Ti-6Al-4V to 304L stainless steel gradient components fabricated with laser deposition additive manufacturing. *Mater Des* 2016;104:404–13. <https://doi.org/10.1016/j.matdes.2016.05.016>.
- [30] Li W, Yan L, Karnati S, Liou F, Newkirk J, Taminger KMB, et al. Ti-Fe intermetallics analysis and control in joining titanium alloy and stainless steel by Laser Metal Deposition. *J Mater Process Technol* 2017;242:39–48. <https://doi.org/10.1016/j.jmatprotec.2016.11.010>.
- [31] Onuike B, Bandyopadhyay A. Functional bimetallic joints of Ti6Al4V to SS410. *Addit Manuf* 2020;31:100931. <https://doi.org/10.1016/j.addma.2019.100931>.
- [32] Tey CF, Tan X, Sing SL, Yeong WY. Additive manufacturing of multiple materials by selective laser melting: Ti-alloy to stainless steel via a Cu-alloy interlayer. *Addit Manuf* 2020;31:100970. <https://doi.org/10.1016/j.addma.2019.100970>.
- [33] Tomashchuk I, Sallamand P. Metallurgical strategies for the joining of titanium alloys with steels. *Adv Eng Mater* 2018;20:1700764. <https://doi.org/10.1002/adem.201700764>.
- [34] Ahmed T, Rack HJ. Phase transformations during cooling in α + β titanium alloys. *Mater Sci Eng, A* 1998;243:206–11.
- [35] Rafi HK, Karthik NV, Gong H, Starr TL, Stucker BE. Microstructures and mechanical properties of Ti6Al4V parts fabricated by selective laser melting and electron beam melting. *J Mater Eng Perform* 2013;22:3872–83. <https://doi.org/10.1007/s11665-013-0658-0>.
- [36] Materials Science International Team MSIT®. Al-Cu-Ti (aluminium - copper - titanium): light metal ternary systems: phase diagrams, crystallographic and thermodynamic Data. In: Effenberg G, Ilyenko S, editors. Light met. Syst. Part 2, 11A2. Berlin, Heidelberg: Springer Berlin Heidelberg; 2005. p. 1–18. https://doi.org/10.1007/10915967_11.
- [37] Raghavan V. Al–Cu–Ti (Aluminum–Copper–Titanium). *J Phase Equilibria Diffus* 2006;27:156–7. <https://doi.org/10.1007/s11669-006-0044-9>.
- [38] Raghavan V. Cu–Fe–Ti (Copper–Iron–Titanium). *J Phase Equil* 2002;23:172. <https://doi.org/10.1361/1054971023604152>.
- [39] Mou G, Hua X, Huang Y, Shen C, Wang M. Study on the microstructure optimization and mechanical properties of dissimilar TC4–304L arc-brazing joints. *Mater Sci Eng, A* 2020;788:139566. <https://doi.org/10.1016/j.msea.2020.139566>.
- [40] Li J, Yu N, Jiang H, Leng J, Geng H. Effects of annealing temperature on dealloying of Ti–Cu Alloy. *Corrosion Sci* 2015;91:95–100. <https://doi.org/10.1016/j.corsci.2014.11.002>.
- [41] Li D, Wang B, Luo L, Li X, Xu Y, Li B, et al. The interface structure and its impact on the mechanical behavior of TiAl/Ti₂AlNb laminated composites. *Mater Sci Eng, A* 2021;827:142095. <https://doi.org/10.1016/j.msea.2021.142095>.
- [42] Tan X, Kok Y, Tan YJ, Descoins M, Mangelinck D, Tor SB, et al. Graded microstructure and mechanical properties of additive manufactured Ti–6Al–4V via electron beam melting. *Acta Mater* 2015;97:1–16. <https://doi.org/10.1016/j.actamat.2015.06.036>.
- [43] Zhang X, Pan T, Flood A, Chen Y, Zhang Y, Liou F. Investigation of copper/stainless steel multi-metallic materials fabricated by laser metal deposition. *Mater Sci Eng, A* 2021;811:141071. <https://doi.org/10.1016/j.msea.2021.141071>.
- [44] Zafari A, Xia K. Laser powder bed fusion of ultrahigh strength Fe–Cu alloys using elemental powders. *Addit Manuf* 2021;47:102270. <https://doi.org/10.1016/j.addma.2021.102270>.
- [45] Wang CP, Liu XJ, Kainuma R, Takaku Y, Ohnuma I, Ishida K. Formation of core-type macroscopic morphologies in Cu–Fe base alloys with liquid miscibility gap. *Metall Mater Trans A* 2004;35:1243–53. <https://doi.org/10.1007/s11661-004-0298-y>.
- [46] Sun X, Hao W, Geng G, Ma T, Li Y. Solidification microstructure evolution of undercooled Cu-15 wt.% Fe alloy

- melt. *Adv Mater Sci Eng* 2018;2018:1–6. <https://doi.org/10.1155/2018/6304518>.
- [47] Wei C, Liu L, Gu Y, Huang Y, Chen Q, Li Z, et al. Multi-material additive-manufacturing of tungsten - copper alloy bimetallic structure with a stainless-steel interlayer and associated bonding mechanisms. *Addit Manuf* 2022;50:102574. <https://doi.org/10.1016/j.addma.2021.102574>.
- [48] Guo C, Li S, Shi S, Li X, Hu X, Zhu Q, et al. Effect of processing parameters on surface roughness, porosity and cracking of as-built IN738LC parts fabricated by laser powder bed fusion. *J Mater Process Technol* 2020;285:116788. <https://doi.org/10.1016/j.jmatprotec.2020.116788>.
- [49] Liu L, Wang D, Deng G, Yang Y, Chen J, Tang J, et al. Interfacial characteristics and formation mechanisms of copper–steel multimaterial structures fabricated via laser powder bed fusion using different building strategies. *Chin J Mech Eng Addit Manuf Front* 2022;100045. <https://doi.org/10.1016/j.cjmeam.2022.100045>.
- [50] Eremenko VN, Buyanov YuI, Prima SB. Phase diagram of the system titanium-copper. *Sov Powder Met Ceram* 1966;5:494–502. <https://doi.org/10.1007/BF00775543>.
- [51] Shie RK, Wu SK, Chan CH, Huang CS. Infrared brazing of Ti-6Al-4V and 17-4 PH stainless steel with a nickel barrier layer. *Metall Mater Trans A* 2006;37:2207–17. <https://doi.org/10.1007/BF02586140>.
- [52] Liao J, Yamamoto N, Liu H, Nakata K. Microstructure at friction stir lap joint interface of pure titanium and steel. *Mater Lett* 2010;64:2317–20. <https://doi.org/10.1016/j.matlet.2010.07.049>.
- [53] Kundu S, Chatterjee S, Olson D, Mishra B. Effects of intermetallic phases on the bond strength of diffusion-bonded joints between titanium and 304 stainless steel using nickel interlayer. *Metall Mater Trans A* 2007;38:2053–60. <https://doi.org/10.1007/s11661-007-9273-8>.
- [54] Elrefaey A, Tilmann W. Solid state diffusion bonding of titanium to steel using a copper base alloy as interlayer. *J Mater Process Technol* 2009;209:2746–52. <https://doi.org/10.1016/j.jmatprotec.2008.06.014>.
- [55] Wang H, Wang L, Cui R, Wang B, Luo L, Su Y. Differences in microstructure and nano-hardness of selective laser melted Inconel 718 single tracks under various melting modes of molten pool. *J Mater Res Technol* 2020;9:10401–10. <https://doi.org/10.1016/j.jmrt.2020.07.029>.
- [56] Wei C, Liu L, Cao H, Zhong X, Xu X, Gu Y, et al. Cu10Sn to Ti6Al4V bonding mechanisms in laser-based powder bed fusion multiple material additive manufacturing with different build strategies. *Addit Manuf* 2022;51:102588. <https://doi.org/10.1016/j.addma.2021.102588>.